International Journal of Microwave and Wireless Technologies

cambridge.org/mrf

Research Paper

Cite this article: Kumar A, Ali M, Gallego DC, Rivera AL, Carpintero G (2026) Dielectric waveguide interconnects for hybrid mm-Waves and terahertz system integration. *International Journal of Microwave and Wireless Technologies*, 1–10. https://doi.org/10.1017/S1759078726103626

Received: 31 December 2025 UTC
Revised: 24 June 2026 UTC
Accepted: 30 June 2026 UTC

Keywords:
contactless coupling; hybrid terahertz system; silicon dielectric waveguides; substrateless integration; terahertz interconnects

Corresponding author: Ashish Kumar;
Email: akumar@ing.uc3m.es

Dielectric waveguide interconnects for hybrid mm-Waves and terahertz system integration

Ashish Kumar[1], Muhsin Ali[2], Daniel Cabo Gallego[2], Alejandro Lavado Rivera[2] and Guillermo Carpintero[1,2]

[1]Optoelectronics and Laser Technology Group, Department of Electronics Technology, Universidad Carlos III de Madrid, Leganés, Madrid, Spain and [2]Leapwave Technologies, Leganés, Madrid, Spain

Abstract

In this work, we propose interconnection structures for substrateless all-silicon dielectric waveguides, a platform for terahertz (THz) hybrid integration that currently relies on traditional tapered interfaces. We demonstrate two dielectric waveguide-to-waveguide interconnect approaches: a truncated termination and a quarter-wave-matched (QWM) slot termination. Both designs maintain a confined coupling point, enabling consistent coupling. Experimental results show maximum interconnection coupling losses of 5 dB and 2.5 dB for the truncated and QWM-slot terminations, respectively, across the 220–330 GHz band. The QWM-slot transmission coefficient remains above -3 dB with a misalignment tolerance up to 100 μm, representing a 2.5$\times$ improvement over the truncated design. Offset characterization along three axes reveals smooth decoupling behavior over a 1 mm range, validating the potential for broadband, contactless interconnects between dielectric waveguide interfaces. These results establish a compact THz interconnect concept with substantially relaxed translational alignment tolerances, making it well-suited for deployment in scalable 6G multi-chip arrays and THz sensing modules.

Introduction

Practical millimeter-wave (mm-Waves) and terahertz (THz) systems require integration platforms that combine low-loss guiding, compactness, and robust packaging. Although conventional hollow metallic waveguides remain prevalent in laboratory settings, their performance at THz frequencies is constrained by Drude loss, tight fabrication tolerances, and mechanically fragile packaging factors that hinder large-scale integration and mass manufacturing [1–3]. These limitations have motivated an extensive shift toward all-dielectric THz waveguides, particularly those based on high-resistivity intrinsic silicon, which offers near-lossless propagation, strong field confinement, and compatibility with mature microfabrication processes [4–6]. In this context, substrateless all-silicon (Si) microstructures have emerged as a promising THz integration platform, enabling low-loss guiding, monolithic integration of diverse components, and simplified packaging within a mechanically robust frame [7–9].

Efficient low-loss THz interconnects have been reported and could be prime candidates for meeting the ever-growing demand for higher data rates in short-range interconnection applications [10, 11]. THz interconnects bridge the gap between board-level links and the limited bandwidth of electrical chip-to-chip connections. These short-range links, typically spanning a few centimeters, are commonly referred to as "last-centimeter interconnects" [11, 12]. Si dielectric THz waveguides have already demonstrated applications toward 6G and beyond, with propagation loss below 0.05 dB/cm and bandwidths on the order of $\sim$350 GHz [13, 14]. Representative all-Si THz waveguide platforms include photonic crystal waveguides, effective-medium (EM) waveguides, and unclad dielectric wire waveguides [7–9]. For comparison, conventional metallic rectangular waveguides in the same frequency range typically exhibit attenuation on the order of 0.5–2 dB/cm, depending on band and surface finish, as can be inferred from standard manufacturer data and attenuation charts for WR-series waveguides. This illustrates that silicon dielectric rectangular waveguides can achieve more than an order of magnitude reduction in propagation loss compared with conventional hollow metallic waveguides, while also offering improved integration and packaging flexibility.

Photonic crystal waveguides can achieve very low loss ($<0.1\ dB/cm$), but their operation bandwidth is typically limited to $\sim$20 GHz due to the inherent constraints of photonic band gap guiding [15, 16]. EM waveguides retain similarly low loss while offering significantly wider bandwidths reported values reach $\sim$120 GHz around 0.3 THz and $\sim$350 GHz in the 1 THz band [13, 14]. However, EM waveguide designs rely on intricate subwavelength perforations that demand high-precision etching, which complicates scaling and limits design flexibility. Unclad all-silicon waveguides have been proposed to relax some of these constraints, they can preserve propagation losses below 0.1 dB/cm with bandwidths comparable to effective-medium platforms [9, 17], while simplifying the microstructure and enabling more straightforward implementation of bends, splitters, and couplers [18, 19]. Collectively, these all-silicon waveguide platforms now provide versatile components for low-loss THz interconnects and functional integrated components [7, 8].

Despite these advances, dielectric waveguides alone do not intrinsically offer the mechanical flexibility required for chip-to-chip or board-to-board interconnections, since they are typically fabricated from high-resistivity crystalline Si with limited bendability. To address this, hollow-core fibers have attracted considerable attention as flexible THz interconnects [20, 21]. More recently, flexible Polytetrafluoroethylene (PTFE)-core solid dielectric waveguides have been explored for mm-Waves applications [22]. In that work, PTFE circular dielectric waveguides with diameters of 0.5 and 1 mm were designed and characterized across the 325–500 GHz band, demonstrating measured transmission losses below 0.3 and 0.33 dB/cm, respectively, and bending losses below 0.01 dB/cm [22]. However, coupling from metallic waveguides via horn-based launchers introduced approximately 3 dB of insertion loss, and segment-to-segment interconnection using PTFE heat shrink tubes added a further 1.6–2.5 dB [22]. Despite their mechanical flexibility, these waveguides are therefore less suitable for low-loss, high-performance THz interconnects.

A notable step forward is the recently demonstrated THz fiber link using a dielectric silicon waveguide interface [23]. In this work, a tapered all-Si dielectric waveguide is employed as an efficient coupler between a THz hollow core fiber and a silicon dielectric waveguide, enabling a 22 Gbit/s link in the 0.3 THz band with a coupling efficiency of ∼60% and a 3 dB bandwidth of 150 GHz over 10 cm of fiber [23]. This result highlights that carefully engineered dielectric couplers can substantially improve interface efficiency and throughput, underscoring the potential of THz interconnects as practical "last-centimeter" links for high-speed, short-range communications. At the same time, it also exemplifies a broader trend in THz integration: most high-performance dielectric interconnects to date still rely on relatively long, carefully shaped tapers or complex couplers whose performance can be sensitive to fabrication tolerances and mechanical misalignment [9, 17, 24]. This motivates compact waveguide-to-waveguide interconnect schemes on substrateless all-Si platforms that preserve low loss and wide bandwidth while improving robustness to misalignment at module-to-module interfaces. From the perspective of practical mm-Waves and THz hybrid integration, the most relevant figures of merit for dielectric waveguide-to-waveguide interconnect schemes are not limited to insertion loss alone, but also include operational bandwidth, interface compactness, and robustness to assembly tolerances. Existing taper-based or fiber-coupled dielectric interfaces can provide efficient coupling, but they often rely on comparatively long transition regions or mechanically demanding alignment conditions [22, 23, 25]. Our approach focuses on a compact termination geometry that supports contactless coupling while enabling a quantifiable tolerance to translational misalignment. The main contribution of the proposed quarter-wave-matched (QWM)-slot interconnect lies not only in its coupling performance across the 220–330 GHz band but also in its combination of a compact footprint and relaxed alignment sensitivity. These features are vital for ensuring repeatable packaging and reliable multi-module assembly at millimeter-wave and THz frequencies. Such characteristics are particularly relevant for modular 6G front-ends and phased-array tiles, where chip-to-module connections must be formed with pick-and-place-level accuracy while remaining robust to vibration and thermal expansion.

An earlier version of this work was presented in the EuMW 2025 Proceedings [26]. This paper extends that preliminary study by providing a comprehensive theoretical framework and an expanded analysis of the results and their significance. We introduce terminations for uncladded silicon dielectric waveguides that facilitate integration with active or passive components to form a complete THz interconnected system, as illustrated in Fig. 1(a). The proposed schemes include two termination types: truncated and QWM-slot, depicted in Fig. 1(b) and (c), respectively. Beyond establishing efficient signal coupling, these designs exhibit high robustness against misalignments arising from positioning tolerances.

Concept

The first design is a truncated waveguide termination, the simplest approach to create an interconnection, where the dielectric waveguide tip is truncated in a flat termination. This termination has been previously reported with dipole antenna and straight forward waveguide-to-waveguide interconnect [27, 28], and generally exhibits high reflection when there is an abrupt change in the effective index of the propagating mode. In practice, high reflection also occurs when connecting two waveguides if a lateral gap forms at the interface due to fabrication tolerances (e.g., variations in waveguide dimensions or over-etching) and finite positioning accuracy. This gap creates a discontinuity that reflects a significant portion of the incident power, reducing interconnection efficiency.

To address these issues, we introduce a QWM-slot termination at the end of the dielectric waveguide. The QWM-slot-terminated dielectric waveguide provides an effective solution by introducing a free-space matching section that minimizes reflection losses and partially compensates for alignment imperfections. A resonant slot region, whose electrical length approximates a quarter of the in-guide wavelength, transforms the impedance seen by the incoming mode and improves modal matching across the interface. [27]. As a result, the QWM-slot approach improves transmission coefficient and mitigates the impact of dimensional variations, gaps, and modal index mismatches that arise in realistic mm-Waves and THz assemblies. We first analyze the transmission losses of two interconnected terminations by simulating two scenarios using CST Microwave Studio, one without offset and the other with an X-axis offset, as illustrated in Fig. 1(b) and (c). The dimensions of the dielectric waveguides and the QWM-slot geometry correspond to the optimized design reported in [27], which was validated through full-wave simulations and measurements over the 220–330 GHz frequency range. We initially position the two dielectric waveguide tips such that their flat terminations are aligned center-to-center (zero offset) to obtain the maximum transmission coefficient. Then, to assess real-world implications, we introduce misalignment along the X-axis, increasing the offset between centers in 1 μm steps, and evaluate the performance of both terminations under these conditions.

The simulated transmission coefficient of perfectly aligned waveguide terminations is shown in Fig. 2(a). The truncated termination exhibits a higher absolute transmission coefficient than the QWM-slot termination over most of the band, with coupling losses of approximately 1.5 dB at 220 GHz and 0.4 dB at 330 GHz. It is important to note that Fig. 2(a) presents the absolute transmission coefficient $|S_{21}|$ under perfect alignment, whereas Fig. 2(b)

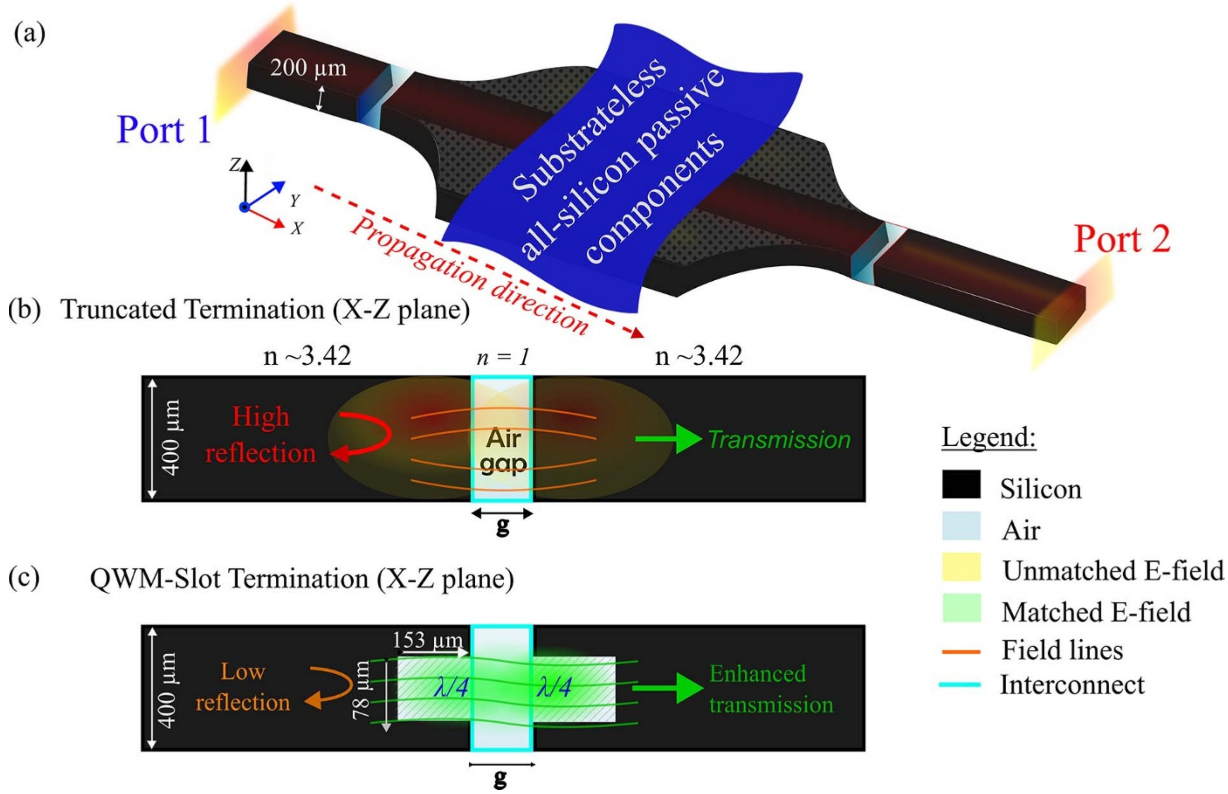

Figure 1. (a) 3D schematic overview of a THz hybrid integrated system featuring substrate-less silicon components connected via dielectric waveguides, with labeled input (Port 1) and output (Port 2). Cross-sectional view (X-Z plane) illustrating the operating principles for: (b) a truncated termination with high reflection at the air gap (g), and (c) the proposed QWM-slot termination showing enhanced transmission through quarter-wavelength ($\lambda/4$) impedance matching structures.

and (c) shows the normalized offset loss, defined as the additional coupling loss relative to the perfectly aligned case (0 μm offset) for each termination design. To evaluate robustness against lateral gap formation, the transmission coefficient is further analyzed as a function of X-axis misalignment, with offsets up to 100 μm. The resulting offset loss is normalized with respect to the perfectly aligned case and is summarized in Fig. 2(b) and (c) for the truncated and QWM-slot terminations, respectively. For the truncated termination Fig. 2(b), the normalized offset loss increases significantly with offset and frequency, exceeding 4 dB at large misalignment. In contrast, the QWM-slot termination Fig. 2(c) maintains substantially lower sensitivity to lateral offsets, with losses generally remaining below 2 dB across most of the investigated frequency and offset range. These results highlight that, although the truncated termination offers superior absolute performance under ideal alignment, the QWM-slot termination provides a much more robust interconnection in realistic scenarios where fabrication tolerances, temperature-induced drift, and instrument-induced vibrations can introduce offsets along all three axes. This distinction allows for a direct comparison of misalignment tolerance, independent of the absolute insertion loss differences observed in Fig. 2(a).

Overcoming these challenges motivates termination designs such as the QWM slot that ensure free-space matching across the operational frequency range, thereby minimizing reflected power and maintaining a high transmission coefficient even under offset conditions. This capability enables seamless integration of silicon dielectric waveguide-based active and passive components for hybrid incorporation into THz systems.

Truncated interconnect

The truncated termination can be interpreted as butt-coupling between two nominally identical dielectric rectangular waveguides separated by a small free-space gap. In the ideal limit of a vanishing gap and perfect lateral alignment, the dominant coupling mechanism is modal overlap between the fundamental modes on the two sides. A standard way to express the transmission coefficient into the fundamental output mode is through a power-normalized mode-overlap (reaction) integral [29, 30]:

$$\eta_{\text{trunc}} \approx \frac{\left|\iint_A (\mathbf{E}_1 \times \mathbf{H}_2^*) \cdot \hat{\mathbf{z}}\, dA\right|^2}{P_1 P_2} \tag{1}$$

where $(\mathbf{E}_1, \mathbf{H}_1)$ and $(\mathbf{E}_2, \mathbf{H}_2)$ are the modal fields in the input and output waveguides, respectively, P_1 and P_2 are the corresponding guided powers, and the integral is evaluated over a transverse plane at the interface. For identical waveguides with negligible gap and perfect alignment, Eq. (1) approaches $P_1 = P_2$, yielding $\eta_{\text{trunc}} \to 1$ (0 dB). In practice, finite gaps and residual offsets reduce the overlap and introduce additional mismatch and radiation; therefore, full-wave simulation is required for accurate prediction.

When a finite gap g is present, the interconnect can be approximated as a short section of free space between two identical guided sections. In a first-order transmission-line (TL) picture as shown in Fig. 3(a), the gap behaves like a section of characteristic impedance $Z_0 \approx 377\,\Omega$ and electrical length $k_0 g$. The input impedance looking into the gap can be written as

$$Z_{\text{in}}(g) = Z_0 \frac{Z_{\text{wg}} + jZ_0 \tan(k_0 g)}{Z_0 + jZ_{\text{wg}} \tan(k_0 g)} \tag{2}$$

https://doi.org/10.1017/S1759078726103626

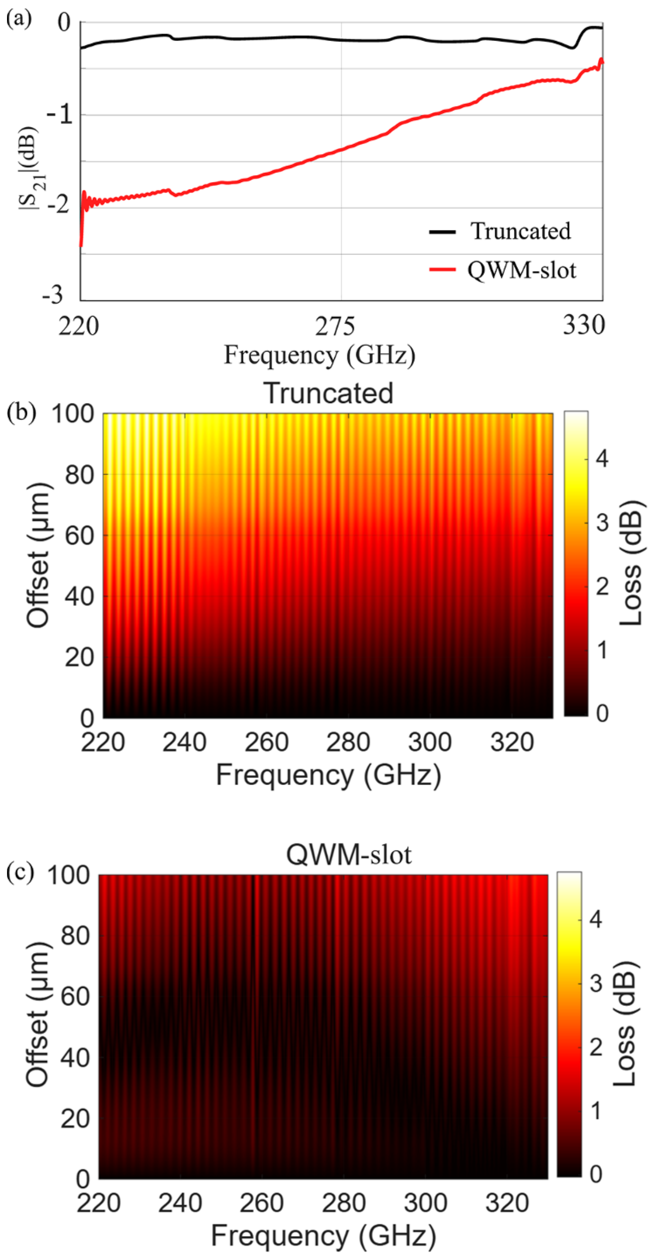

Figure 2. Simulated transmission coefficient $|S_{21}|$ for perfectly aligned (a), and additional offset loss introduced by X-axis offset with respect to perfect alignment for truncated (b) and QWM-slot (c).

where Z_{wg} denotes the (modal) characteristic impedance of the dielectric-waveguide fundamental mode and $k_0 = 2\pi/\lambda_0$ is the free-space wavenumber. The corresponding reflection coefficient at the waveguide reference plane is

$$\Gamma_{\mathrm{trunc}}(g) = \frac{Z_{\mathrm{in}}(g) - Z_{\mathrm{wg}}}{Z_{\mathrm{in}}(g) + Z_{\mathrm{wg}}} \tag{3}$$

From Eqs. (2) and (3), Γ_{trunc} is intrinsically periodic versus frequency (through $\tan(k_0 g)$), producing a ripple consistent with the wavy components observed in both simulation and measurement, as illustrated in Fig. 3(a). Importantly, the TL model does not capture radiation loss and near-field coupling in the gap; therefore, it is used here to provide physical intuition for the interference-driven ripple, while the absolute insertion loss and the full offset dependence are obtained from full-wave CST simulations and measurements.

Lateral misalignment further reduces coupling by decreasing the field correlation between the two modal profiles. A microwave-friendly approximation expresses the offset-dependent coupling as a normalized cross-correlation of the transverse fields,

$$\eta_{\mathrm{offset}}(\Delta x) \approx \frac{\left| \iint_A \left(\mathbf{E}_t(x,y) \cdot \mathbf{E}_t^*(x-\Delta x, y) \right) \mathrm{d}A \right|^2}{\left(\iint_A |\mathbf{E}_t(x,y)|^2 \mathrm{d}A \right)^2} \tag{4}$$

where $\mathbf{E}_t$ is the transverse modal electric field. For small offsets, a second-order expansion yields the expected smooth (approximately Gaussian-like) decay, but Eq. (4) avoids assuming an optical Gaussian beam and remains consistent with guided-wave mode matching.

The CST results in Fig. 2(b) show that offsets up to 100 μm can induce several dB of additional loss for the truncated termination. This motivates a misalignment-tolerance comparison between the two designs, since practical assemblies cannot guarantee sub-10 μm repeatability.

QWM-slot interconnect

The QWM-slot termination introduces a sub-wavelength slot cavity at the waveguide end that acts as a compact impedance-transforming section between the high-index guided mode and the effective load presented by the gap plus the receiving waveguide. Using a simplified TL analogy illustrated in Fig. 3(b), the interface can be interpreted as

$$Z_{\mathrm{wg}} \to Z_{\mathrm{slot}} \to Z_{\mathrm{load}} \tag{5}$$

If the slot electrical length is close to a quarter guided wavelength,

$$\ell_{\mathrm{slot}} \approx \frac{\lambda_{\mathrm{g,slot}}}{4} \tag{6}$$

then the classical quarter-wave transformer relation gives the input impedance

$$Z_{\mathrm{in,slot}} \approx \frac{Z_{\mathrm{slot}}^2}{Z_{\mathrm{load}}} \tag{7}$$

Using Eq. (7), the approximate matching condition becomes [Fig. 3(b)]

$$Z_{\mathrm{wg}} \approx \frac{Z_{\mathrm{slot}}^2}{Z_{\mathrm{load}}} \tag{8}$$

As in the truncated case, this TL picture is intended as a first-order interpretation; the QWM-slot interconnect also involves radiation and near-field interaction that are not included in Eqs. (6)–(8). Consequently, the geometry is optimized using full-wave simulations, and the TL model is used to explain why the slot reduces the effective mismatch and smooths sensitivity to gap/offset.

01 The reflection coefficient implied by the equivalent input impedance is

$$\Gamma_{\mathrm{QWM}} \approx \frac{Z_{\mathrm{in,slot}} - Z_{\mathrm{wg}}}{Z_{\mathrm{in,slot}} + Z_{\mathrm{wg}}} \tag{9}$$

Eq. (9) connects directly to the port reflection via $S_{11} \approx \Gamma$ in the single-mode regime. In practice, deviations arise due to radiation and higher-order fields localized near the slot, and therefore agreement is assessed against full-wave S-parameters (Figs. 2 and 6). The key experimental outcome is that, while the truncated termination can provide slightly lower loss under perfect alignment, the

https://doi.org/10.1017/S1759078726103626

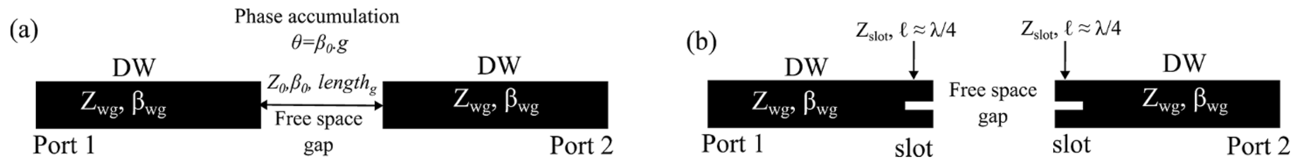

Figure 3. Transmission-line models of the proposed dielectric-waveguide interconnects: (a) truncated interface with a free-space gap, where phase accumulation ($\theta = \beta_0 * g$) causes transmission ripple; (b) back-to-back QWM-slot interconnect, where Z_{slot} and $\ell \approx \lambda/4$ improve impedance matching and reduce reflections.

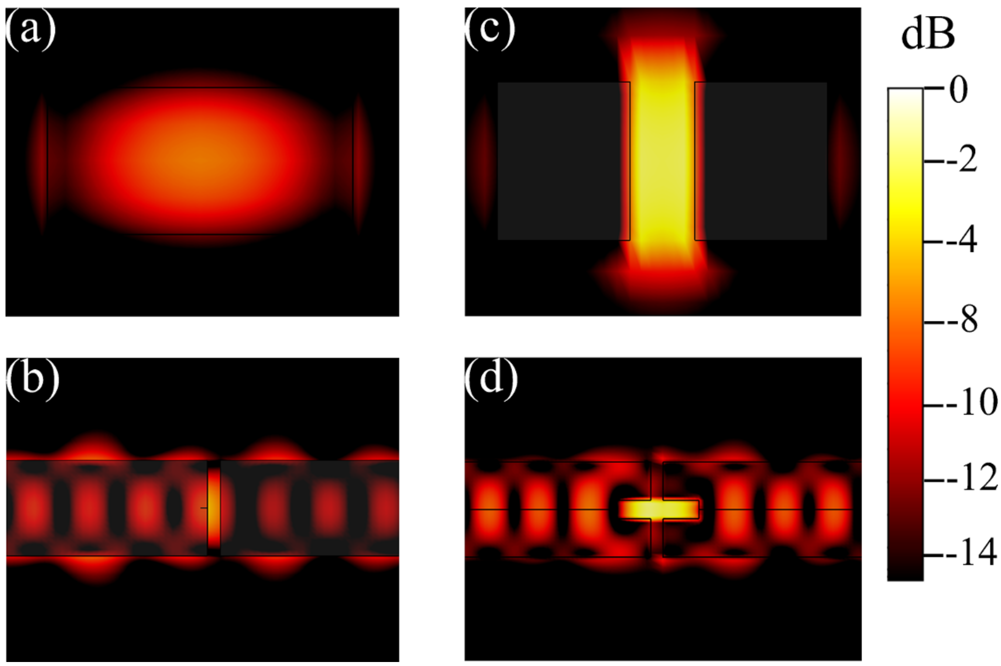

Figure 4. Simulated $|E|$ near the interface at 275 GHz for (a,b) truncated and (c,d) QWM-slot terminations under identical gap/offset conditions. The QWM-slot confines and redistributes the field within the coupling region, improving misalignment tolerance.

QWM-slot termination provides substantially larger misalignment tolerance (e.g., 100 μm at the -3 dB threshold), which is the more relevant figure of merit for hybrid-integrated assemblies.

Full-wave CST simulations show that the QWM slot supports a localized standing-wave pattern in the slot region, where the stored electric and magnetic energies are redistributed such that the net reactive component seen from the waveguide is minimized. One practical way to identify the quarter-wave condition numerically is to monitor the input reflection coefficient S_{11} at the waveguide port as a function of slot length, and to select the geometry that minimizes $|S_{11}|$ near the target frequency. Alternatively, from the $|E|$ field distribution shown in Fig. 4, the progression of the dominant field component inside the slot, e.g., E_x along the slot axis, can be used to estimate the effective guided wavelength $\lambda_{\text{g,slot}}$. The slot length can then be adjusted until the phase shift across the slot approaches $\pi/2$ at the frequency of interest.

When two QWM-slot terminations are placed face-to-face with a finite lateral offset, the localized field in each slot still couples predominantly into the fundamental mode of the opposing waveguide, as long as the overlap between the slot apertures remains appreciable. Unlike the truncated case, the presence of the resonant slot reduces the sensitivity of the effective impedance to the exact gap size and lateral alignment. In other words, the QWM slot provides an intermediate matching region that partially "buffers" geometrical perturbations, so that the input sees a relatively stable impedance even under moderate misalignment. This behavior is evident in Fig. 2(c), where the QWM-slot termination exhibits significantly lower additional loss than the truncated case, with values generally remaining below 2 dB over the investigated offsets and frequencies.

In summary, while the truncated termination offers the highest transmission coefficient under perfect alignment, the QWM-slot termination provides significantly improved robustness against realistic misalignments and gap formation. By exploiting quarter-wave impedance transformation in a compact slot geometry, the QWM slot maintains low reflection and high transmission coefficient over the operating band, enabling reliable dielectric-waveguide interconnects for practical THz modules and systems.

Measurement

The two sets of silicon dielectric waveguide samples were fabricated using deep reactive ion etching (DRIE). Each sample was terminated on one end with either a truncated or a QWM-slot waveguide, forming the interconnect under test, while the opposite end incorporated a 4 mm linear taper to interface the dielectric waveguide with a metallic hollow waveguide. For this transition, a cyclic olefin copolymer (COC) holder structure [31] with a circular flange-style alignment was designed to support and position the silicon waveguide. While this study focuses on translational offsets along the X, Y, and Z axes, it is noted that angular misalignments, though not explicitly investigated here, may also occur in practical

https://doi.org/10.1017/S1759078726103626

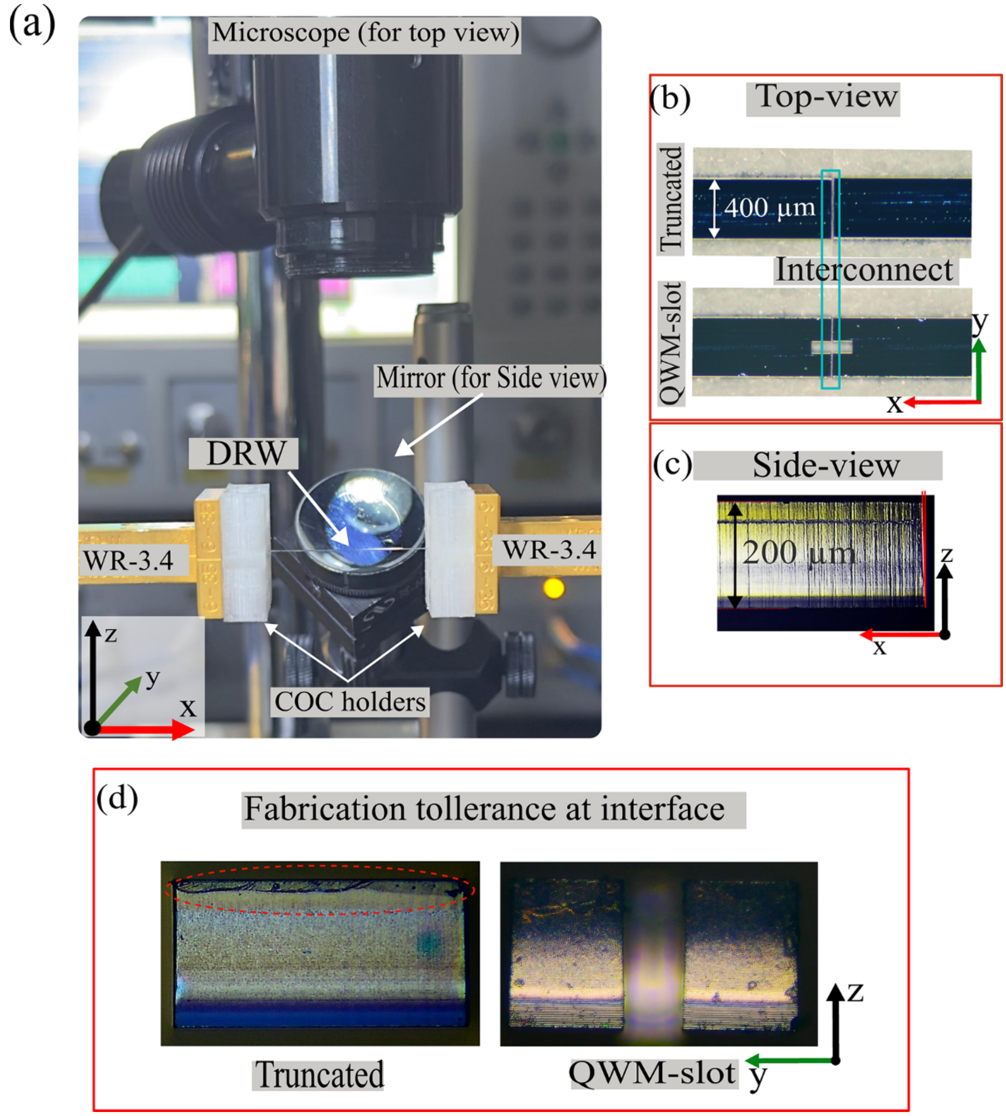

Figure 5. (a) Photograph of experimental setup, Microscopic image, (b) top view, (c) side view, and (d) fabrication tolerance at interconnect.

packaging. Nevertheless, translational tolerance remains the primary metric for robustness in pick-and-place assembly and modular THz integration, where positional placement errors typically dominate the alignment budget. Measurements were performed using an Anritsu VectorStar vector network analyzer (VNA) with Virginia Diodes WR-3.4 (220–330 GHz) frequency extension modules equipped with hollow metallic waveguide ports. The experimental setup is shown in Fig. 5(a), with an inset highlighting the silicon waveguide mounted on its COC holder. A standard SOLT (Short–Open–Load–Thru) calibration was used to shift the reference plane to the hollow waveguide interface, and all results were normalized to the coupling response of a straight silicon dielectric waveguide terminated with 3 mm tapers on both ends. An optical microscope was used to monitor the relative alignment of the two silicon waveguides during measurements, and motorized translation stages were employed to introduce and quantify controlled offsets, enabling accurate evaluation of the offset-dependent transmission coefficient. To account for residual offsets arising from fabrication over-etching and finite positioning resolution, the coupling coefficient was also simulated assuming a 50 μm lateral offset, ensuring a fair comparison between measurement and simulation.

Figure 6 presents a comprehensive comparison of the normalized simulated and measured S-parameters for both interconnect terminations across the 220–330 GHz band. Figure 6(a) shows the transmission coefficient $|S_{12}|$, where the QWM-slot termination (red) achieves an average insertion loss of approximately −2.5 dB with relatively flat spectral response and peak transmission approaching −2 dB near 275 GHz. In contrast, the truncated termination (black) exhibits higher insertion loss, averaging around −4 dB with pronounced frequency-dependent variations reaching −5 dB near 280 GHz. The simulated response (dashed black line) for the truncated case shows better performance (-2.5 to -3 dB), indicating that the measured degradation is primarily due to fabrication tolerances and assembly misalignment.

The reflection coefficient $|S_{11}|$ in Fig. 6(b) reveals that both terminations maintain good return loss across the band. The truncated termination shows measured reflection levels between -13 and -16 dB, with the simulated response (dashed black) predicting slightly different performance (-11 to -12 dB). The QWM-slot

https://doi.org/10.1017/S1759078726103626

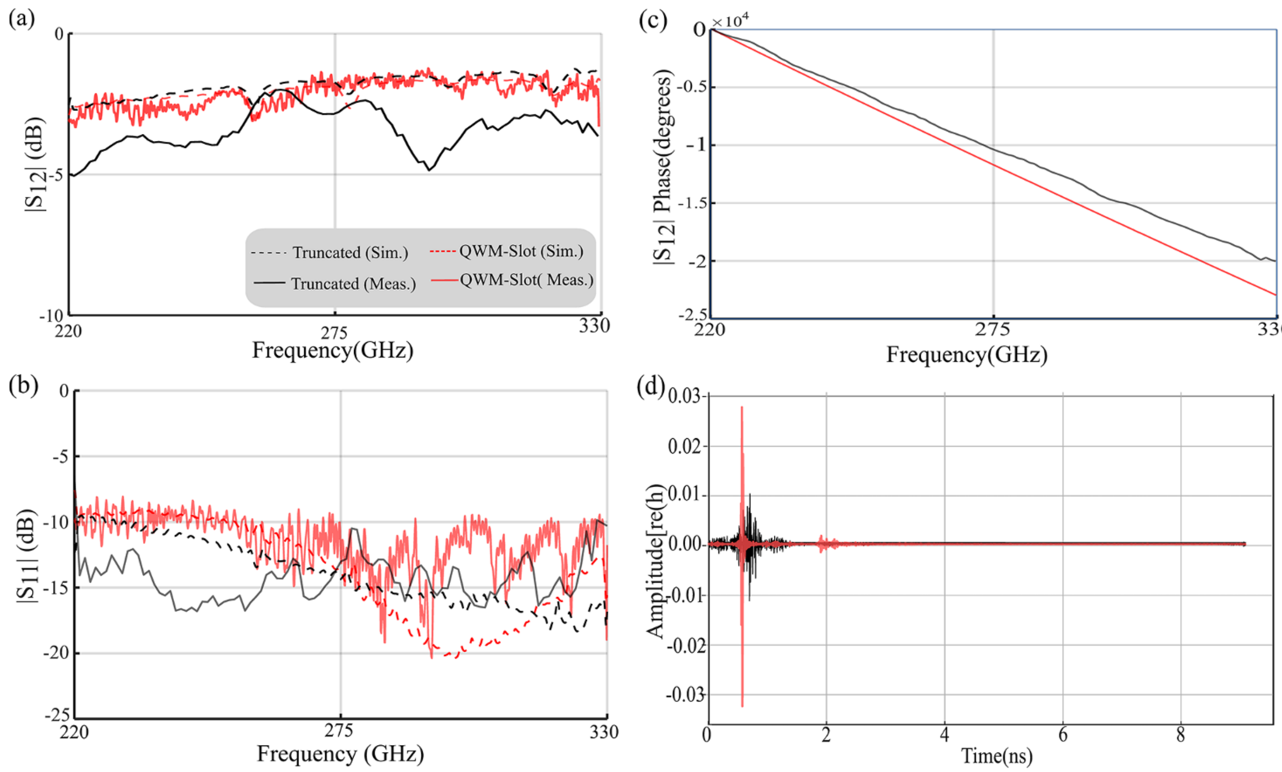

Figure 6. Comparison of simulated and measured S-parameters and signal integrity metrics for the truncated and QWM-slot interconnect designs (a) Transmission coefficient ($|S_{12}|$), (b) reflection coefficient ($|S_{11}|$), (c) transmission phase response ($\angle S_{12}$), and (d) time-domain impulse response $h(t)$. Dashed lines represent simulations while solid lines denote experimental measurements.

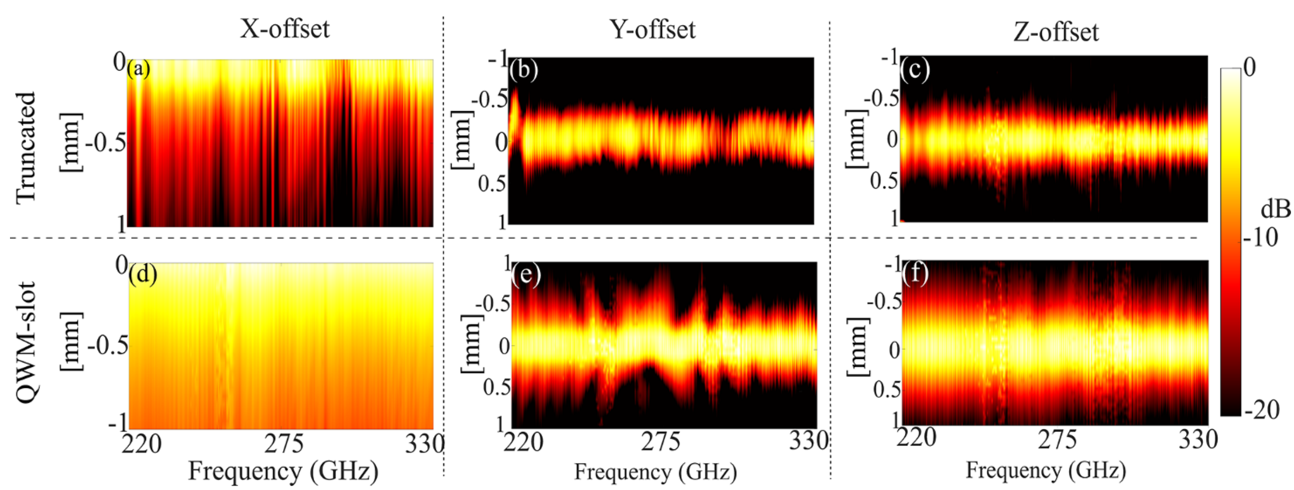

Figure 7. Coupling response under lateral misalignment for truncated (a–c) and QWM-slot (d–f) interconnects. The offset is defined relative to the nominal aligned configuration (0 mm). (a,d) x-offset (longitudinal separation), (b,e) y-offset (vertical shift), and (c,f) z-offset (transverse lateral shift).

termination demonstrates superior reflection suppression, with measured values consistently below −9 dB and reaching −10 dB around 260 GHz. The simulated QWM-slot response (dashed red) shows even better matching, with reflection levels approaching −20 dB near 280 GHz, confirming the effectiveness of the quarter-wave impedance transformation in minimizing interface mismatch.

Figure 6(c) displays the transmission phase $\angle S_{12}$ as a function of frequency. Both terminations exhibit nearly linear phase progression, characteristic of propagation delay through the interconnect structure. The QWM-slot (red) shows a phase variation from approximately 0° at 220 GHz to $-2.310\times^{4\circ}$ at 330 GHz, while the truncated termination (black) follows a similar trend with a slightly steeper slope, ranging from 0° to approximately $-2.0\times^{4\circ}$. The linear phase response confirms minimal dispersion and indicates that both interconnects preserve signal integrity across the operational bandwidth.

The time-domain impulse response in Fig. 6(d) is obtained via inverse Fourier transform of the measured S-parameters. Both terminations produce a sharp main pulse centered near 0.5 ns,

https://doi.org/10.1017/S1759078726103626

with the QWM-slot (red) exhibiting a peak amplitude of approximately 0.028 [rel.] and the truncated termination (black) showing a slightly lower peak of about 0.008 [rel.]. The QWM-slot demonstrates cleaner temporal characteristics with reduced ringing and lower residual reflections beyond 2 ns, consistent with its superior impedance matching observed in the frequency domain. The truncated termination shows more pronounced secondary reflections between I0 ns and 1 ns, attributed to impedance discontinuities at the waveguide interface. Both responses decay to negligible levels beyond 2 ns, confirming that the interconnects introduce minimal temporal distortion and are suitable for high-speed data transmission applications. The QWM-slot exhibits good agreement between simulation and measurement, whereas larger deviations are observed for the truncated termination when compared to the ideal, perfectly aligned simulated case in Fig. 2(a). These discrepancies are attributed to misalignment between the interconnected waveguides, clearly visible in both top and side microscope views. As highlighted by the red dotted circles, fabrication over-etching and assembly tolerances introduce residual offsets that degrade the transmission coefficient and increase insertion loss. Due to inherent fabrication tolerances and limitations of positioning systems in practical THz assemblies, such misalignments are unavoidable. To quantify their impact, the transmission efficiency was evaluated as a function of offset along the X, Y, and Z directions. The measured attenuation maps, with performance quantified from 0 to -20 dB, are presented in Fig. 7 for the truncated (a–c) and QWM-slot (d–f) terminations. For a more application-oriented comparison, the offset values corresponding to signal losses of −3 dB, −6 dB, and −10 dB were extracted, as these thresholds represent meaningful degradations in link budget and system reliability. The resulting tolerance levels are summarized in Table 1. Notably, the −3 dB tolerance of 100 μm achieved by the QWM-slot termination (Table 1) falls within typical placement capability for automated assembly, supporting packaging-centric use cases such as modular sub-THz front-ends and array interconnects. The QWM-slot interconnect achieves a measured −6 dB tolerance of 240 μm (Table 1), which is significantly larger than typical silicon etching misalignments ($\pm 50\ \mu$m) and assembly errors in THz systems ($\pm 100\ \mu$m). While the offsets introduced in the laboratory are predominantly translational and idealized, practical modules also exhibit angular and rotational misalignments. Although angular misalignments were not explicitly investigated in this experimental study, the extended coupling region of the QWM-slot is expected to reduce sensitivity to general assembly imperfections, thereby suggesting a more robust framework for the packaging and integration of THz modules.

Table 1. Evaluated misalignment thresholds for −3, −6, and −10 dB signal attenuation levels. Values correspond to the frequency-averaged transmission coefficient over the 220–330 GHz band

Interconnect	Axis	−3 dB	−6 dB	−10 dB
Truncated	X	–	200 μm	400 μm
	Y	–	200 μm	200 μm
	Z	–	200 μm	300 μm
QWM-slot	X	100 μm	240 μm	450 μm
	Y	100 μm	240 μm	400 μm
	Z	100 μm	240 μm	450 μm

Table 2. Comparison of representative contactless or interface-oriented mm-Waves or THz interconnect approaches

Technology	Band (GHz)	Loss (dB)	Tolerance	Footprint	CF[1]
Fiber–Si interface [23]	220–330	∼2.2	Sensitive	Large	Yes
Two-conductor port [25]	220–500	<2.0	N/A[2]	Large	No
Truncated Si-DWG [28]	220–330	∼4.5	<50 μm	Compact	Yes
Trunc. & QWM [26]	220–330	5.0 / 2.5	Qualitative	Compact	Yes
QWM-slot (this work)	**220–330**	**∼2.5**	**100 μm**	**Sub-λ**	**Yes**

Note: [1]CF: Contactless Facilitation (ability to maintain performance across a physical gap). [2]N/A: Not applicable (metal-assisted port, not a gap-based interconnect).

Conclusion

To contextualize the performance of the proposed interconnects within the broader THz integration, Table 2 benchmarks the QWM-slot termination against the most relevant dielectric and metallic interconnection technologies previously reported. In this work, we have proposed and experimentally demonstrated dielectric waveguide terminations for robust interconnection in hybrid-integrated THz systems. In particular, a QWM slot termination enables a compact, contactless interface between substrateless all-silicon dielectric waveguides. Compared to the conventional truncated interconnect [28], the QWM-slot termination improves the peak interconnection coupling by approximately 2.5 dB across the 220–330 GHz band and maintains a −3 dB coupling tolerance up to 100 μm. The three-axis offset characterization further reveals smooth and predictable decoupling over a separation range of approximately 1 μm. While angular and rotational tolerances remain an important subject for future investigation, the demonstrated three-axis translational robustness already addresses the dominant alignment errors encountered in practical hybrid-integrated sub-THz modules.

Beyond the measured performance gains, the QWM slot provides two complementary physical benefits that are central to its robustness. First, it acts as an impedance-matching element, reducing the effective reflection at the interface via a QWM-slot termination [27]. Second, it redistributes the fields into an extended slot aperture, which relaxes the sensitivity to translational offsets and provides leverage in practical packaging and assembly. Together, these effects yield a compact and packaging-tolerant interconnect concept for substrateless silicon dielectric waveguides. A specific application of the proposed QWM-slot interconnect is the contact-free, short-reach routing of sub-THz signals in modular 6G front-ends or multi-chip modules (MCMs). For instance, it can interface a packaged transmitter/receiver IC with a passive all-silicon dielectric-waveguide distribution network feeding a phased-array antenna tile. In such assemblies, thermal expansion, mechanical vibration, and pick-and-place placement errors make sub-10 μm alignment unrealistic. The measured translational tolerance of up to 100 μm at the −3 dB threshold (Table 1), combined with the compact sub-λ footprint, enables repeatable module-to-module assembly with relaxed translational alignment requirements. This packaging-oriented approach directly addresses the practical "last-centimeter" interconnect challenges in scalable 6G hardware and high-throughput THz sensing modules.

https://doi.org/10.1017/S1759078726103626

Acknowledgements. Funding for APC: Universidad Carlos III de Madrid (Agreement CRUE-Madroáo 2026).

Funding statement. This work was supported by the European Union's Horizon Europe research and innovation program through the Services Joint Undertaking projects SPRINTER (Grant Agreement No. 101070581), TERA6G (Grant Agreement No. 101096949), and POLYNICES (Grant Agreement No. 101070549).

Additional support was provided by the Spanish Ministry of Science and Innovation (MICIU) and the State Research Agency (AEI) through the national grant MiBiLab (ref. PID2023-149035OB-I00), co-funded by ERDF/UE.

Alejandro Lavado Rivera and Daniel Cabo Gallego acknowledge support from the *Ayudas para contratos Torres Quevedo* program of the Spanish State Research Agency (grant No. PTQ2022-012580 and No. PTQ2022-012583, respectively).

This work also received funding from the Spanish Ministry of Economic Affairs and Digital Transformation and the European Union NextGenerationEU through the project "TERAcom-6G" (ref. TSI-064100-2023-39) within the UNICO I+D 5G-6G 2023 program for research infrastructure and scientific equipment and the EPIC-Pack project (TSI-069100-2023-6).

Competing interests. The authors report no conflict of interest.

References

1. **Siegel PH** (2002) Terahertz technology. *IEEE Transactions on Microwave Theory and Techniques* **50**(3), 910–928.
2. **Kleine-Ostmann T and Nagatsuma T** (2011) A review on terahertz communications research. *Journal of Infrared, Millimeter, and Terahertz Waves* **32**(2), 143–171.
3. **Headland D, Monnai Y, Abbott D, Fumeaux C and Withayachumnankul W** (2018) Tutorial: Terahertz beamforming, from concepts to realizations. *APL Photonics* **3**(5), 051101.
4. **Mendis R and Grischkowsky D** (2001) Undistorted guided-wave propagation of subpicosecond terahertz pulses. *Optics Letters* **26**(11), 846–848.
5. **Wächter M, Nagel M and Kurz H** (2009) Tapered photoconductive terahertz field probe tip with subwavelength spatial resolution. *Applied Physics Letters* **95**(4), 041112.
6. **Jianqiang M, Shrestha R, Adelberg J, Yeh C-Y, Hossain Z, Knightly E, Jornet JM and Mittleman DM** (2018) Security and eavesdropping in terahertz wireless links. *Nature* **563**(7732), 89–93.
7. **Headland D, Fujita M, Carpintero G, Nagatsuma T and Withayachumnankul W** (2023) Terahertz integration platforms using substrateless all-silicon microstructures. *APL Photonics* **8**(9), 091101.
8. **Ratmalgre ASDK, Fujita M and Nagatsuma T** (2022a) Nanophotonics-inspired all-silicon waveguide platforms for terahertz integrated systems. *Nanophotonics* **11**(9), 1741–1759.
9. **Headland D, Withayachumnankul W, Xiongbin Y, Fujita M and Nagatsuma T** (2020) Unclad microphotonics for terahertz waveguides and systems. *Journal of Lightwave Technology* **38**(24), 6853–6862.
10. **Nagatsuma T, Ducournau G and Renaud CC** (2016) Advances in terahertz communications accelerated by photonics. *Nature Photonics* **10**(6), 371–379.
11. **Song H-J and Nagatsuma T** (2011) Present and future of terahertz communications. *IEEE Transactions on Terahertz Science and Technology* **1**(1), 256–263.
12. **Yu B, Liu Y, Ye Y, Liu X and Qun Jane G** (2016) Low-loss and broadband g-band dielectric interconnect for chip-to-chip communication. *IEEE Microwave and Wireless Components Letters* **26**(7), 478–480. https://doi.org/10.1109/LMWC.2016.2574837
13. **Gao W, Xiongbin Y, Fujita M, Nagatsuma T, Fumeaux C and Withayachumnankul W** (2019) Effective-medium-cladded dielectric waveguides for terahertz waves. *Optics Express* **27**(26), 38721–38734.
14. **Ratmalgre ASDK, Fujita M and Nagatsuma T** (2022b) Ultra-low-loss and broadband all-silicon dielectric waveguides for WR-1 band (0.75–1.1 THz) modules. *Photonics* **9**(8), 515.
15. **Ishigaki T, Fujita M, Nagai M, Ashida M and Nagatsuma T** (2012) Photonic-crystal slab for terahertz-wave integrated circuits. In *IEEE Photonics Conference 2012*. IEEE, pp. 774–775.
16. **Yata M, Fujita M and Nagatsuma T** (2016) Photonic-crystal diplexers for terahertz-wave applications. *Optics Express* **24**(7), 7835–7849.
17. **Headland D and Carpintero G** (2025) Robust unclad terahertz waveguides and integrated components enabled by multimode effects and matched slot couplers. *IEEE Transactions on Terahertz Science and Technology* **15**(5), 885–893.
18. **Headland D, Gallego DC, Sakaki M, Benson N and Carpintero G** (2025) Multi-octave all-dielectric directional coupler using integrated half-mirror for ultrawideband terahertz systems. *Laser & Photonics Reviews* **19**, 2401644.
19. **Gao W, Fujita M, Murakami S, Nagatsuma T, Fumeaux C and Withayachumnankul W** (2025) Ultra-wideband terahertz integrated polarization multiplexer. *Laser & Photonics Reviews* **19**(1), 2400270.
20. **Bowden B, Harrington JA and Mitrofanov O** (2007) Silver/polystyrene-coated hollow glass waveguides for the transmission of terahertz radiation. *Optics Letters* **32**(20), 2945–2947.
21. **Lai C-H, Hsueh Y-C, Chen H-W, Huang Y-J, Chang H-C and Sun C-K** (2009) Low-index terahertz pipe waveguides. *Optics Letters* **34**(21), 3457–3459.
22. **Hao L, Zhang D and Zhu H** (2024) PTFE-based circular terahertz dielectric waveguides. In *Photonics*, Vol. 11, MDPI, p. 921.
23. **Koala R, Iyoda K, Gao W, Matsuura Y, Fujita M and Nagatsuma T** (2023) Terahertz fiber link using dielectric silicon waveguide interface. *Optics Express* **31**(5), 7351–7362.
24. **Amarloo H and Safavi-Naeini S** (2021) Enhanced on-chip terahertz vibrational absorption spectroscopy using evanescent fields in silicon waveguide structures. *Optics Express* **29**(11), 17343–17352.
25. **Headland D, Gallego DC and Carpintero G** (2024a) Two-conductor ports enabling broadband operation of substrateless microscale silicon waveguides. *IEEE Transactions on Terahertz Science and Technology* **14**(4), 543–547.
26. **Kumar A, Ali M, Headland D, Rivera-Lavado A and Carpintero G** (2025) Dielectric waveguide-based interconnects for integrated mm-wave and terahertz systems. In *2025 55th European Microwave Conference (EuMC)*. IEEE, pp. 65–68.
27. **Headland D, Kumar A, Lees H, Withayachumnankul W and Carpintero G** (2024b) Matched dielectric slot waveguide as an all-dielectric terahertz magnetic dipole. *Optics Letters* **49**(5), 1361–1364.
28. **Ichikawa D, Gao W, Ngo NH, Ohara T, Tanaka M, Murakami S, Yamada Y, Yamane H, Nishida Y, Fujita M and Nagatsuma T** (2025) Terahertz on-chip communications with hybrid electronic-photonic interconnects. *IEEE Transactions on Terahertz Science and Technology* **15**(5), 751–762.
29. **Marcatili EAJ** (1969) Dielectric rectangular waveguide and directional coupler for integrated optics. *Bell System Technical Journal* **48**(7), 2071–2102.
30. **Westerveld WJ, Leinders SM, van Dongen KWA, Urbach HP and Yousefi M** (2012) Extension of Marcatili's analytical approach for rectangular silicon optical waveguides. *Journal of Lightwave Technology* **30**(14), 2388–2401.
31. **Cai L, Jiang ZH, Jing-Bo W, Chen H and Hong W** (2023) Low-loss and flexible terahertz bandpass frequency selective surface based on cyclic olefin copolymer substrate via solvent-free synthesis. *Optics Express* **31**(13), 21706–21720.

Ashish Kumar received his Master's degree in Optical Engineering from Nanjing University of Science and Technology, China, and his Bachelor's degree in Electrical and Electronics Engineering from Vel Tech Dr. Rangarajan Dr. Sagunthala R&D Institute of Science and Technology, India. From 2021 to 2024, he was a Marie Skłodowska-Curie Actions Fellow in the TERAOPTICS network, undertaking research secondments at the Center for Physical Sciences and Technology (FTMC), Vilnius, Lithuania. His research interests include terahertz system design, simulation and analysis, dielectric waveguides and waveguide-to-waveguide interconnects.

Muhsin Ali received the B.S. degree in telecommunications engineering from NUCES, Islamabad, Pakistan, in 2011, the M.S. degree in electrical engineering from NUST, Islamabad, in 2013, and the Ph.D. degree in electrical, electronics and automation engineering Universidad Carlos III de Madrid (UC3M), Madrid, Spain, in 2020. He was a Visiting Researcher with Fraunhofer Heinrich Hertz Institute, Berlin, Germany, in 2019, and the University of Duisburg-Essen, Duisburg, Germany in 2021. He is the co-founder and RF Lead at LeapWave Technologies, a deep-tech company based in Madrid. Currently, he focuses on developing ultra-broadband interconnect technology for instrumentation, sensing and wireless systems markets. His research interests include the design, fabrication and integration aspects of mmWave and THz emitters and detectors for high-speed wireless links with beam-steering capability.

Daniel cabo Gallego received the B.S. degree in physics and the M.S. degree in optoelectronics from the Universidad de Santiago de Compostela, Santiago, Spain, in 2003, and the Ph.D. degree in electronics engineering from Universidad Carlos III de Madrid (UC3M), Madrid, Spain, in 2016. Since 2022, he is a Co-Founder and led the Photonic Department, LeapWave Technologies, Leganés, Spain. His research interests include terahertz photonics and their applications to sensing and imaging, optoacoustic imaging systems for biomedical applications, high-power short-pulse diode laser instrumentation, optical fiber sensors, and optical detection and generation of high-frequency ultrasounds.

Alejandro Lavado Rivera was born in Madrid, Spain, in October 24, 1984. He received the Engineering degree in telecommunications and the Ph.D. (cum laude) degree in communications from Universidad Carlos III de Madrid (UC3M), Madrid, in 2010 and 2016, respectively. From 2018 to 2022, he was with Yebes Observatory, Dirección General del Instituto Geográfico Nacional, Yebes, Spain. Since 2022, he has been the Chief Technology Officer with LeapWave Technologies, Leganés, Spain. His research interests include dielectric lenses, ultra-broadband terahertz antennas, low-loss terahertz transmission lines, and radio astronomy instrumentation.

Guillermo Carpintero(Senior Member, IEEE) received the Telecommunication Engineering degree from the Universidad Politécnica de Madrid (UPM), Madrid, Spain, 1994, and the Ph.D. degree from the Universidad Carlos III de Madrid (UC3M), Madrid, in 1999. He is currently a Professor with the Electronics Technology Department, UC3M, and the Co-Director of the Optoelectronics and Laser Technology Group (GOTL). He has participated in technical program committees of numerous scientific conferences (ECOC, IRMMW-THz, MWP). His research interests include integrated microwave photonics, hybrid photonic integration, integrated mode-locked lasers, photonic-enabled beam-steered array antennas, integrated Terahertz technology, and high-frequency packaging. Prof. Carpintero research outcome was recognized with several research awards and distinctions, including the "Doctoral Thesis Extraordinary Award" from UC3M in 2000, "Heather Williamson Young Investigator Award" from International Society for Optics and Photonics in 2000, the UC3M Social Council Excellence Award in 2009, and the 2011 Best European research and Development Project in Cooperation Award from Madri+d Foundation.

https://doi.org/10.1017/S1759078726103626